Visible-Light Photocatalysis of ZnO Deposited on Nanoporous Au

Masataka Hakamada*[,a], Motohiro Yuasa[b], Takashi Yoshida[a], Fumi Hirashima[a] and Mamoru Mabuchi[a]

[a] Graduate School of Energy Science, Kyoto University, Yoshidahonmachi, Sakyo, Kyoto 606-8501, Japan.

[b] Materials Research Institute for Sustainable Development, National Institute of Advanced Industrial Science and Technology (AIST), 2266-98 Anagahora, Shimoshidami, Moriyama, Nagoya 463-8560, Japan.

Abstract. ZnO deposited on nanoporous Au showed photocatalytic decomposition toward methyl orange (MO) under visible light, unlike ZnO sputtered on flat Au without a nanoporous structure. First-principle calculations suggested that the surface lattice disorder in nanoporous Au induced a band gap narrowing and a large built-in electric field in the adjacent ZnO, resulting in the visible light photocatalytic response.

Keywords: zinc oxide; interface; photocatalysis; band gap; first-principles calculations

1. Introduction

Zinc oxide (ZnO) is a direct band gap semiconductor (band gap = 3.37 eV), and has received much interest because of its optical and electronic properties. It has applications in piezoelectric nanogenerators [1], solar cells [2], gas sensors [3] and photocatalysts [4–6]. ZnO is an important photocatalyst because of its high photosensitivity and stability [4–6]. Most semiconductor photocatalysts including ZnO have band gaps in the ultraviolet (UV) region (band gap $\geq$ 3.2 eV, λ < 387 nm), and so promote photocatalysis upon UV irradiation. The solar spectrum consists of only 5–7% UV, with the remaining 46 and 47% consisting of visible and infrared wavelengths, respectively [7]. Various techniques can allow semiconductor photocatalysts to absorb lower energy photons. These include surface modification via organic molecules and semiconductor coupling, band gap modification by creating oxygen vacancies and oxygen sub-stoichiometry, co-doping with nonmetals, and doping with metals and nonmetals [8–11].

Nanoporous metals can be fabricated by dealloying [12–14] and exhibit surface lattice disorder which influences surrounding deposits [15–17]. Herein, ZnO was sputtered on nanoporous Au to modify its band structure, and its photocatalytic capacity under visible

light was evaluated. The mechanism for the enhanced ZnO photocatalysis is discussed based on first-principles calculations.

2. Experimental methods

Au (> 99.9 mass %) and Ag (> 99.9 mass %) ingots were arc-melted together in an Ar atmosphere, to prepare a precursor $Au_{0.35}Ag_{0.65}$ alloy ingot. After homogenization at 1173 K for 24 h in an Ar atmosphere and subsequent cold rolling, the nanoporous Au substrate was prepared by dealloying of the alloy (free corrosion) at 263 K for 15 h in 70 mass % HNO_3. A flat Au substrate without a nanoporous structure was also prepared by polishing Au plate with 1 μm polycrystalline diamond paste.

ZnO was deposited on nanoporous Au substrates by radio-frequency (RF) magnetron sputtering. A ZnO target was used for sputtering on 10×10 mm^2 Au substrates. A 90% Ar 10% O_2 atmosphere was used for the reaction. The sputtering RF power and pressure were 200 W and 0.3 Pa, respectively. Sputtering was conducted for 80 s at 295 K, yielding a 5–10 nm thick ZnO film.

Microstructures of ZnO sputtered on nanoporous Au were observed by scanning electron microscopy (SEM). X-ray diffraction (XRD, X'Pert Pro by PANalytical, operated under a parallel beam configuration with Cu radiation) analyses were also

conducted to determine the crystallographic feature in the samples. X-ray photoelectron spectroscopy (XPS) using Al Kα radiation ($h\nu$ = 1486.6 eV) elucidated surface elemental compositions. Binding energies were referenced to that of Au-$4f_{7/2}$ at 84.0 eV.

For photocatalysis measurements, samples were immersed in 20 mL of 2×10^{-5} mol/L methyl orange (MO) solution, at 323 K. MO is an azo dye commonly used in the textiles industry, and is considered a good probe material for evaluating photocatalysis. Eight blue fluorescent lamps (20 W, Toshiba Lighting & Technology) were used as the irradiation source, providing a total illumination intensity of 4060 Lux. A UV-cutoff filter (λ < 400 nm) prevented direct excitation by UV wavelengths; the UV-cutoff property of the filter is shown in Figure 1. The solution MO concentration as a function of irradiation time was measured by monitoring the MO absorbance at its wavelength of maximum absorption (λ_{max} = 466.5 nm), using a UV-Vis absorption spectrometer (UV-3100 Shimadzu, Japan).

3. Computational methods

The electronic properties of ZnO deposited on Au were investigated by first-principles calculations. Unfortunately, as shown later, our XRD measurement resulted in no definitive epitaxial characteristics of Au/ZnO interfaces probably due to very small

thickness of ZnO layer; thus Au(111)/ZnO(0001) model was constructed as a representative. Geometric optimization calculations were performed using the Cambridge serial total energy package (CASTEP) [18], in which density-functional theory (DFT) [19,20] was used with a plane-wave basis set. The ensemble DFT scheme [21] was adopted to provide the efficiency necessary for a large metallic system and the width of the Gaussian smearing was 0.1 eV. The exchange-correlation interactions were calculated using the spin-polarized ferromagnetic version of the generalized gradient approximation, according to Perdew et al. [22] To improve the description of the semicore 3d state and the band gap in ZnO, the GGA+U method [23,24] was adopted (U = 6.0 eV), [25,26] where U is the on-site Coulomb interaction correction. Ultrasoft pseudopotentials [27] represented in reciprocal space were used for all elements in the calculations. The cut-off energy was 500 eV [28,29], and the Brillouin zone was sampled using a Monkhorst-Pack 10×10×1 *k*-point mesh.

The atomic configuration for the calculations is shown in Figure 2. To simulate the Au lattice strain often observed in nanoporous Au surfaces, a face-centered cubic Au (111) surface model with 9 Au layers and no ZnO layers was first strained by changing the atomic spacing by ±5% within the (110) plane and subsequent geometrical optimization. The bottom 6 layers were fixed, and the top 3 layers were relaxed. Eight layers of ZnO

were then stacked on the top surface of the 9 Au layers, to form a Au/ZnO/vacuum model with a Au(111)/ZnO(0001) interface. In the stacking, the Au layers were treated as the substrate, and the (10−10) lattice spacing of the ZnO layers was set to match the Au (110) lattice spacing. This was because SEM indicated the deposited ZnO was very thin (discussed later). The thickness of the vacuum layer was set to >10 Å in all experiments. This was sufficient to eliminate interaction between the adjusting cells. Geometrical optimization calculations were conducted again, and revealed that atoms at the Au/ZnO interface (Au-Zn or Au-O) were in several epitaxial configurations with a local minimum energy. Energy calculations on geometrically-optimized Au/ZnO/vacuum and Au/OZn/vacuum models, which had Au-Zn and Au-O contacts respectively, indicated the Au/ZnO/vacuum configuration was more stable than that of the Au/OZn/vacuum model (Table 1). The total energy was minimized when Zn atoms were located in fcc or hcp hollow sites. Thus, models of the Au/ZnO/vacuum with Zn atoms in hcp and fcc hollow sites were considered and referred to as "Au/ZnO" in this paper. For comparison, a bulk ZnO model with 32 Zn and O atoms without Au or vacuum layer was also subjected to the calculation. A cut-off energy of 500 eV and *k*-point mesh of 5×5×3 were used. All models were calculated with periodic boundary conditions.

4. Results and discussion

SEM images, XRD patterns and XPS results of samples are shown in Figures 3–5. Nanoporous Au had an average pore diameter of 8 nm, as determined by image analyses of >100 pores. The SEM image of ZnO-sputtered nanoporous Au (Figure 3b) was similar to that of unsputtered nanoporous Au (Figure 3a), perhaps because the sputtered layer was very thin (5–10 nm). XRD patterns (Figure 4) shows only peaks of Au and no peaks of crystalline ZnO even from the ZnO-sputtered sample due to the ultrasmall thickness of ZnO. Zn (Zn-$2p_{3/2}$ to 1021.6 eV and Zn-$2p_{1/2}$ to 1045.0 eV) was detected by XPS (Figure 5), suggesting the formation of a ZnO thin film on the nanoporous Au, although the stoichiometry of the sputtered ZnO was not clear because of adsorbed contaminating oxygen species (perhaps water and gaseous O_2) on nanoporous Au. Au and residual Ag were also detected, suggesting partial coverage and/or particulate deposition of ZnO, although the SEM images show no information on the deposition state of ZnO.

Logarithmic plots of MO concentration variation with time upon visible light irradiation are shown in Figure 6a. Unsputtered and ZnO-sputtered nanoporous Au significantly reduced the MO concentration. Nanoporous Au by itself has been reported to discolor MO solution, but the discoloration by nanoporous Au is differentiated from

photocatalytic decomposition because nanoporous Au can discolor MO solution even under a dark condition [30]. ZnO-sputtered nanoporous Au exhibited a more significant decrease in MO concentration than unsputtered nanoporous Au. Thus, ZnO promoted MO decomposition when deposited on nanoporous Au. ZnO on flat Au (without a nanoporous structure) had no effect on MO concentration. Thus, ZnO sputtered on nanoporous Au exhibited visible light photocatalysis, while ZnO sputtered on flat Au did not. Figure 6b shows the MO solution appearance immediately after sample immersion. The solution surrounding ZnO-sputtered nanoporous Au turned red (arrowed), indicating the fast decomposition of MO into acids (e.g. benzenesulfonic acid), lowering the solution pH.

Bulk ZnO generally has no photocatalytic activity under visible light excitation. However, the electronic properties of materials are very sensitive to microstructure. Small crystal grains can induce quantum confinement, point defects can create localized states within band gaps, and crystal strains can induce band edge shifts [31–33]. Also, ZnO lattice expansion and contraction can affect its band gap [34,35]. However, a change in ZnO lattice parameter does not necessarily give rise to visible light photocatalytic activity because ZnO on flat Au had no effect on MO concentration. A surface lattice strain of ±5% has been reported in nanoporous metals [16,17,36]. Deposits on nanoporous Au substrates have been suggested to possess a more complex lattice disorder than that of

nanoporous Au substrates [15]. Therefore, it is suggested that the lattice strain of nanoporous Au plays an important role in visible light photocatalysis of ZnO on Au.

First-principles calculations on a Au/ZnO/vacuum atomic model showed lattice expansion along the [0001] *c*-axis in ZnO layers up to 10% on a strained Au (111) surface, as summarized in Table 2. Figure 7 shows the density of states (DOS) of Zn and O in the ZnO layer on strained and unstrained Au (111) surfaces. DOS of bulk ZnO (without Au or vacuum layers) are also shown for comparison. All DOS for Au/ZnO exhibited pseudogaps or metal-induced gap states in the conductive bands (0–5 eV) [25], while those for bulk ZnO exhibited a clear band gap above the Fermi level. Au/ZnO models had their DOS in conductive bands red-shifted compared with those in bulk ZnO. In other words, pseudogaps become narrower in the Au/ZnO model than in bulk ZnO. Inspection of Figure 7 reveals that an expanded Au lattice caused a shift of the state in the conductive band to higher energy, which broadened the pseudogap; however, in the case of contracting the Au lattice, the state above the Fermi level increased while that just below was unchanged, and therefore, the pseudogap was narrower, compared with those for expanded Au and non-strained Au. Thus, lattice contraction in Au decreases band gap in ZnO.

[0001] expansive strain in ZnO has been reported to decrease the band gap [35,38], which the present calculations agree with. A smaller band gap benefits visible light photocatalysis, and ZnO deposited on strained Au enhanced the photocatalytic activity by narrowing the pseudogap. Thus, surface lattice contraction in nanoporous Au was responsible for the visible light photocatalysis of deposited ZnO, because the nanoporous metals contained both expansion and contraction within their surface lattice disorder [16,36].

In numerous photocatalysts composed of nanostructured semiconductor oxides and metallic nanoparticles, photocatalysis is enhanced because photogenerated electrons transfer to the metallic nanoparticles. Thus, electrons avoid recombination with holes, forming stable radicals from separated electrons and holes [39–41]. Electron transfer from oxides to metals is affected by the built-in electric field of the oxide, which governs the tunneling current for the transfer. Table 2 shows the built-in electric field within the ZnO layer, calculated by double macroscopic averages of the potential energy [28,29,37]. Both expansion and contraction within the Au lattice increased the built-in electric field, regardless of Zn position at the interface. It was a remarkable change affecting electronic mobility across the Au/ZnO interface, when considering the exponential dependence of tunneling current on potential energy.

The increase in built-in electric field within the ZnO layer facilitated the transfer of excited electrons from ZnO to Au. The non-rectified electron transfer from ZnO to Au required Ohmic contact between Au and ZnO. Whether the Au/ZnO interface possessed Ohmic or Schottky contacts was unclear, because the work function of ZnO is sensitive to measurement conditions and difficult to determine [42]. The CASTEP code employed herein also cannot specify Schottky barriers unlike previous studies [28] because the energy difference between the double-averaged potential and valence band edge of bulk wurtzite ZnO [28] cannot be calculated. However, several studies on nanostructured ZnO/metallic nanoparticle composite suggest an Ohmic nature of the metal/ZnO interface. [39–41]. Combining semiconductor ZnO with a strained nanoporous Au surface to form heterogeneous structures can promote the separation of photogenerated charge carriers, and increase their lifetime.

Of course, the present enhancement in the degradation of MO solution should not be merely to the Au/ZnO interface; for example, possible damage in nanoporous Au during ZnO sputtering may modify the catalytic properties of Au itself. Thus, the present atomic simulation can only offer the possibility of modification in ZnO bandgap structure and built-in electric field, not giving total understanding of the mechanism. Other various

analyses (i. e. epitaxy of Au/ZnO), such as reflection high-energy electron diffraction technique, are necessary for further elucidation.

5. Summary

ZnO sputtered on nanoporous Au exhibited photocatalytic activity, in the degradation of aqueous MO under visible light excitation. First-principles calculations suggested that surface lattice contraction within nanoporous Au sufficiently narrowed the deposited ZnO pseudogap, to enable a visible light response. The change in lattice constant at the surface of nanoporous Au induced a built-in electric field within the deposited ZnO layer. This resulted in visible light photocatalysis and an increased lifetime of photogenerated holes and electrons. These two factors resulted in strained Au/ZnO interfaces exhibiting visible light photocatalysis, because the Au/ZnO interface is very large due to the intrinsic high surface area of nanoporous Au.

Acknowledgments

First-principles calculations and sample preparation were supported by JSPS Grant-in-Aid for Scientific Research (B) 23360305 and for Young Scientists (B) 24760572, respectively.

References

1. Z. L. Wang, J. Song, Science **312**, 242 (2006)

2. M. Law, L. E. Greene, J. C. Johnson, R. Saykally, P. D. Yang, Nat. Mater. **4**, 455 (2005)

3. J. Zhang, S. Wang, M. Xu, Y. Wang, B. Zhu, S. Zhang, W. Huang, S. Wu, Cryst. Growth Des. **9**, 3532 (2009)

4. E. S. Jang, J.-H. Won, S.-J. Hwang, J.-H. Choy, Adv. Mater. **18**, 3309 (2006)

5. T.-J. Kuo, C.-N. Lin, C.-L. Kuo, M. H. Huang, Chem. Mater. **19**, 5143 (2007)

6. C. Ye, Y. Bando, G. Shen, D. Golberg, J. Phys. Chem. B **110**, 15146 (2006)

7. T. Bak, J. Nowotny, M. Rekas, C. C. Sorrell, Int. J. Hydrogen Energy **27**, 991 (2002)

8. S. Rehman, R. Ullah, A. M. Butt, N. D. Gohar, J. Hazard. Mater. **170**, 560 (2009)

9. A. Fujishima, X. Zhang, D. A. Tryk, Surf. Sci. Rep. **63**, 515 (2008)

10. F. Pan, C. Song, X. J. Liu, Y. C. Yang, F. M. Zeng, Mater. Sci. Eng. R **62**, 1 (2008)

11. T. L. Thompson, J. T. Yates, Jr., Chem. Rev. **106**, 4428 (2006)

12. A. J. Forty, Nature **282**, 597 (1979)

13. A. J. Forty, P. Durkin, *Philos. Mag.* **42**, 295 (1980)

14. J. Erlebacher, M. J. Aziz, A. Karma, N. Dimitrov, K. Sieradzki, Nature **410**, 450 (2001)

15. M. Hakamada, F. Hirashima, M. Takahashi, T. Nakazawa, M. Mabuchi, J. Appl. Phys. **109**, 084315 (2011)

16. M. Hakamada, M. Takahashi, T. Furukawa, K. Tajima, K. Yoshimura, Y. Chino, M. Mabuchi, Phys. Chem. Chem. Phys. **13**, 12277 (2011)

17. T. Fujita, P. Guan, K. McKenna, X. Lang, A. Hirata, L. Zhang, T. Tokunaga, S. Arai, Y. Yamamoto, N. Tanaka, Y. Ishikawa, N. Asao, Y. Yamamoto, J. Erlebacher, M. Chen, Nat. Mater. **11**, 775 (2012)

18. M. C. Payne, M. P. Teter, D. C. Allan, T. A. Arias, J. D. Joannopoulos, Rev. Mod. Phys. **64**, 1045 (1992)

19. P. Hohenberg, W. Kohn, Phys. Rev. **136**, B864 (1964)

20. W. Kohn, L. Sham, Phys. Rev. **140**, A1133 (1965)

21. N. Marzari, D. Vanderbilt, M. C. Payne, Phys. Rev. Lett. **79**, 1337 (1997)

22. J. P. Perdew, K. Burke, M. Ernzerhof, Phys. Rev. Lett. **77**, 3865 (1996)

23. V. Anisimov, J. Zaanen, O. K. Andersen, Phys. Rev. B **44**, 943 (1991).

24. S. L. Dudarev, G. A. Botton, S. Y. Savrasov, C. J. Humphreys, A. P. Sutton, Phys. Rev. B **57**, 1505 (1998)

25. C. L. Dong, C. Persson, L. Vayssieres, A. Augustsson, T. Schmitt, M. Mattesini, R. Ahuja, C. L. Chang, J.-H. Guo, Phys. Rev. B **70**, 195325 (2004)

26. L. L. Jensen, J. T. Muckerman, M. D. Newton, J. Phys. Chem. C **112**, 3439 (2008)

27. D. Vanderbilt, Phys. Rev. B **41**, 7892 (1990)

28. L. Dong, S. P. Alpay, J. Appl. Phys. **111**, 113714 (2012)

29. G. Zhang, X. Luo, Y. Zheng, B. Wang, Phys. Chem. Chem. Phys. **14**, 7051 (2012)

30. M. Hakamada, F. Hirashima, M. Mabuchi, Catal. Sci. Technol. **2**, 1814 (2012)

31. S. Dutta, S. Chattopadhyay, A. Sarkar, M. Chakrabarti, D. Sanyal, D. Jana, Prog. Mater. Sci. **54**, 89 (2009)

32. J. Wang, P. Liu, X. Fu, Z. Li, W. Han, X. Wang, Langmuir **25**, 1218 (2009)

33. Y. Zheng, C. Chen, Y. Zhan, X. Lin, Q. Zhang, K. Wei, J. Zhu, Y. Zhu, Inorg. Chem. **46**, 6675 (2007)

34. H. P. He, F. Zhuge, Z. Z. Ye, L. P. Zhu, F. Z. Wang, B. H. Zhao, J. Y. Huang, J. Appl. Phys. **99**, 023503 (2006)

35. R. Ghosh, D. Basak, S. Fujihara, J. Appl. Phys. **96**, 2689 (2004)

36. M. Hakamada, H. Nakano, T. Furukawa, M. Takahashi, M. Mabuchi, J. Phys. Chem. C **114**, 868 (2010)

37. Y. Dong, L. J. Brillson, J. Electron. Mater. **37**, 743 (2008)

38. F. Zhu-Ge, Z.-Z. Ye, L.-P. Zhu, J.-G. Lü, B.-H. Zhao, J.-Y. Huang, Z.-H. Zhang, L. Wang, Z.-G. Ji, J. Cryst. Growth **268**, 163 (2004)

39. Y. Zheng, L. Zheng, Y. Zhan, Z. Lin, W. Zheng, K. Wei, Inorg. Chem. **46**, 6980 (2007)

40. X. Wang, X. Kong, Y. Yu, H. Zhang, J. Phys. Chem. C **111**, 3836 (2007)

41. T.-H. Yang, L.-D. Huang, Y.-W. Harn, C.-C. Lin, J.-K. Chang, C.-I. Wu, J.-M. Wu, Small **9**, 3169 (2013)

42. K. Jacobi, G. Zwicker, A. Gutmann, Surf. Sci. **141**, 109 (1984)

Table 1. Total energy of Au/ZnO/vacuum and Au/OZn/vacuum models after geometrical optimization.

Model	Strain in Au	Atom (Zn or O) position at interface	Total energy (eV)
Au/ZnO/vacuum		Zn at fcc hollow site	−25397.8
Au/ZnO/vacuum	+0.05	Zn at hcp hollow site	−25397.7
Au/OZn/vacuum		O at atomic top site	−25397.5
Au/ZnO/vacuum		Zn at fcc hollow site	−25400.5
Au/ZnO/vacuum	0.00	Zn at hcp hollow site	−25400.5
Au/OZn/vacuum		O at atomic top site	−25400.3
Au/ZnO/vacuum		Zn at fcc hollow site	−25391.7
Au/ZnO/vacuum	−0.05	Zn at hcp hollow site	−25391.7
Au/OZn/vacuum		O at atomic top site	−25391.4

Table 2. Results of first-principles calculations on Au/ZnO models, showing relationship between strain in Au and ZnO, and ZnO built-in electric field

Zn position at interface	Fractional change in lattice spacing of Au (110)	Average fractional change in lattice spacing in ZnO (0001)	Built-in electric field in ZnO (V/nm)
fcc hollow site	+0.05	0.064	0.404
	0.00	0.095	0.175
	−0.05	0.133	0.424
hcp hollow site	+0.05	0.061	0.445
	0.00	0.098	0.043
	−0.05	0.128	0.263

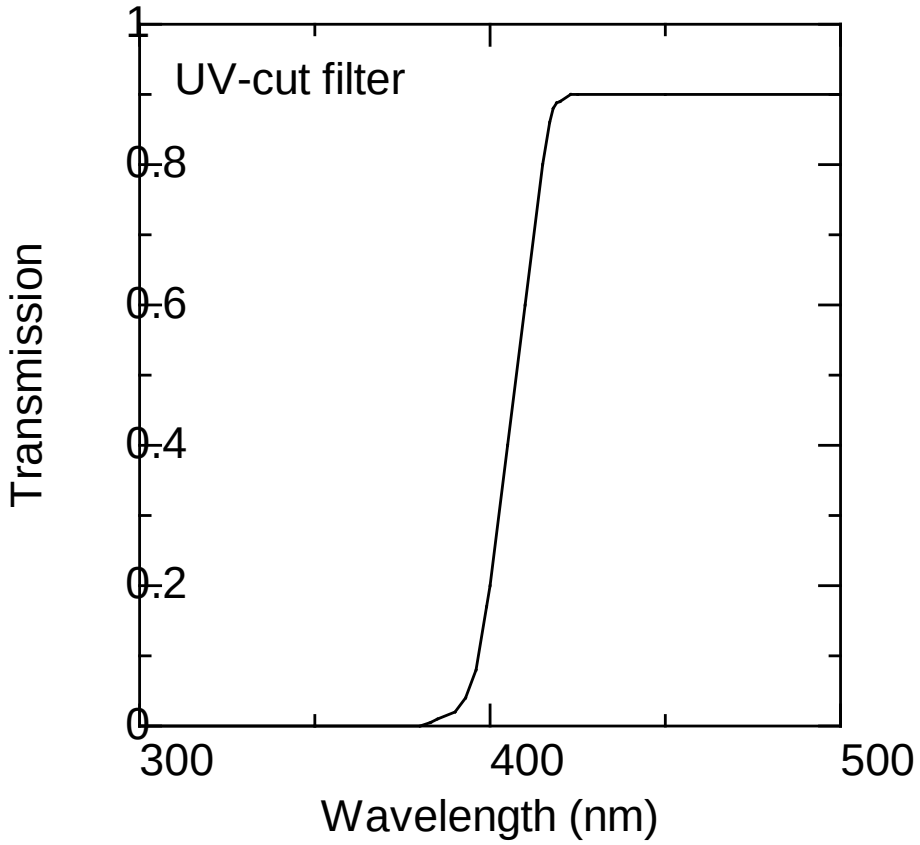

Figure 1. Transmission characteristics of UV-cutoff filter.

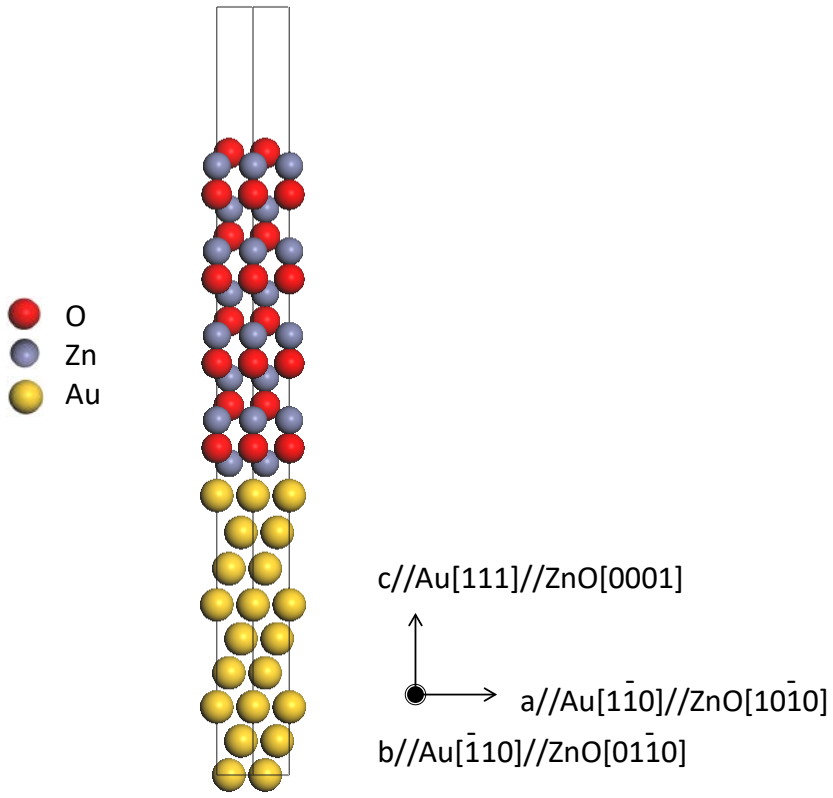

Figure 2. Atomic configuration of Au(111)/ZnO(0001)/vacuum models.

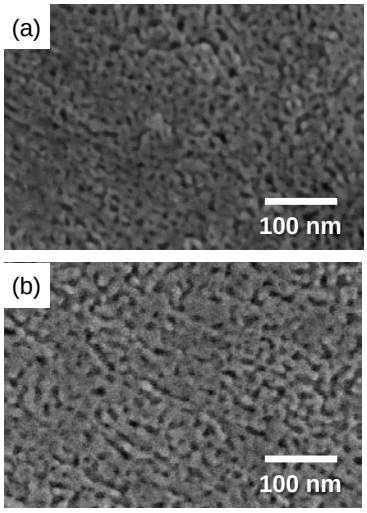

Figure 3. SEM images of nanoporous Au (a) before and (b) after sputtering of ZnO.

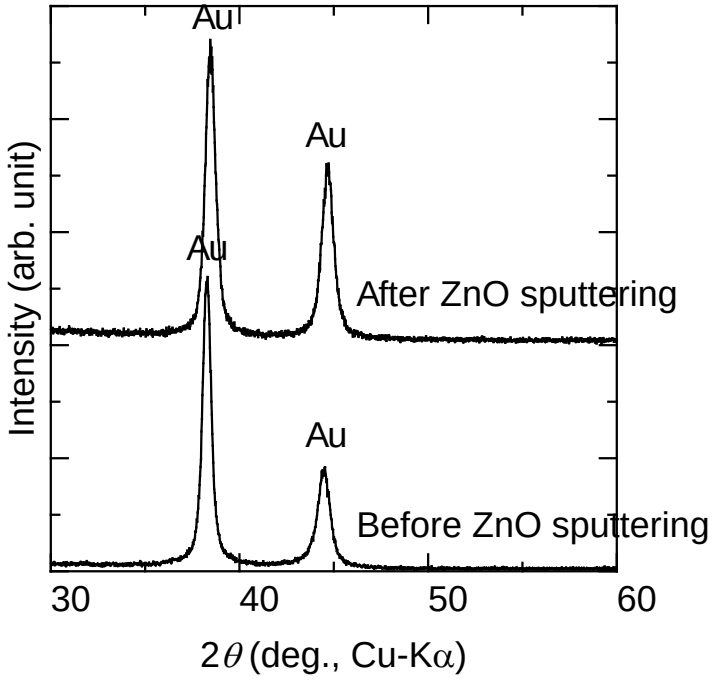

Figure 4. XRD patterns of nanoporous Au before and after sputtering of ZnO.

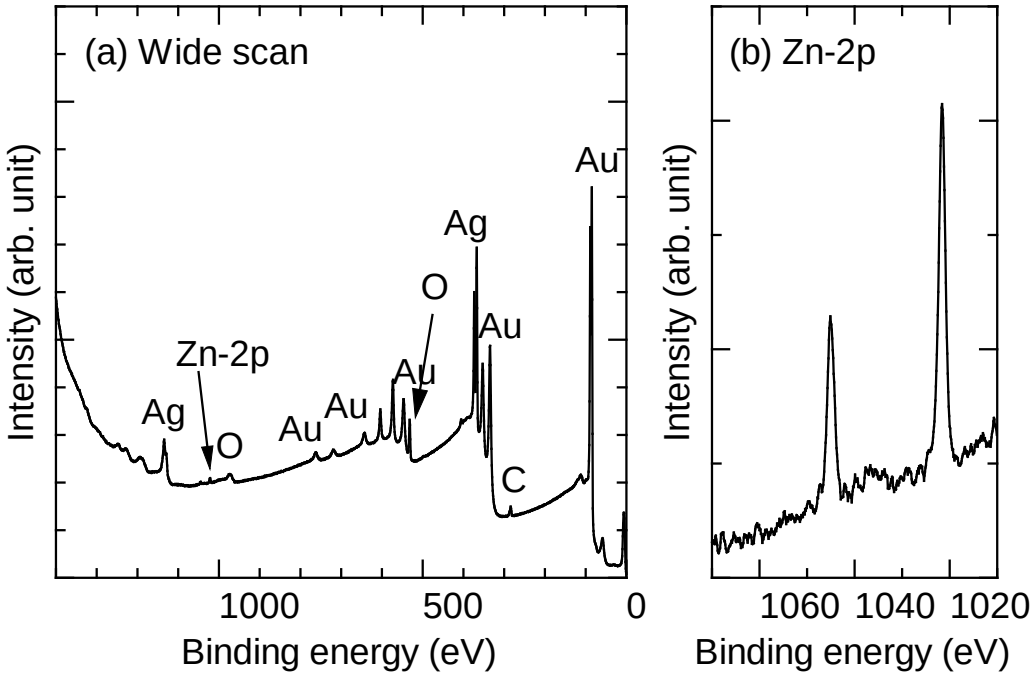

Figure 5. XPS spectrum of nanoporous Au after sputtering of ZnO.

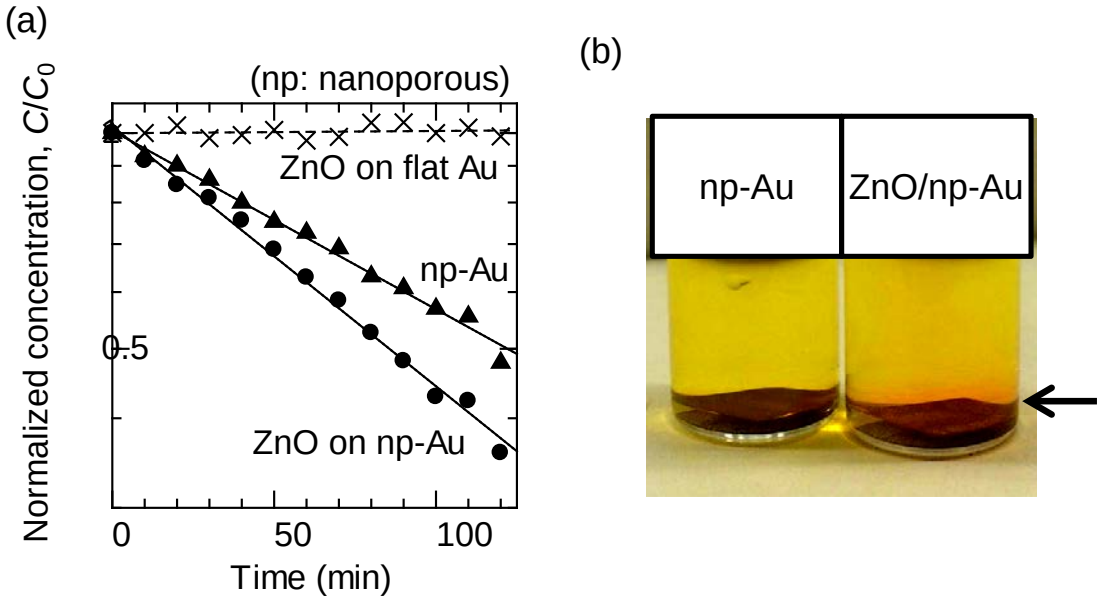

Figure 6. (a) MO concentration variation with time after sample immersion. (b) MO solution appearance immediately after immersion of nanoporous Au with and without ZnO sputtering. The former immediately turned the surrounding solution red, suggesting the rapid decomposition of MO.

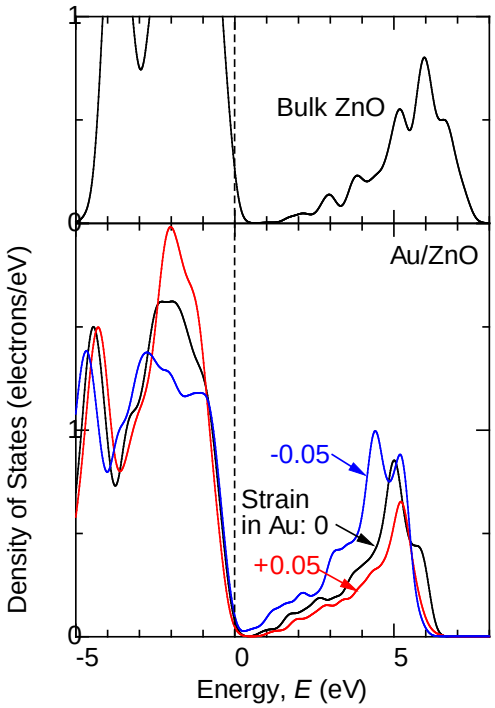

Figure 7. DOS of ZnO for bulk ZnO and Au/ZnO models. Pseudogaps in Au/ZnO were narrower than that in bulk ZnO. The narrowest pseudogap was obtained when the Au lattice contracted by 5%.